Dipole-Tunneling Model from Asymmetric Domain-Wall Conductivity in $LiNbO_3$ Single Crystals

S. Y. Xiao,[1,2] T. Kämpfe,[2] Y. M. Jin,[1] A. Haußmann,[2] X. M. Lu,[1,3] and L. M. Eng[2,4,*]

[1]*Physics School, Nanjing University, Hankou Road 22, 210093 Nanjing, P. R. China*
[2]*Institute of Applied Physics, School of Physics, Technische Universität Dresden, Nöthnitzer Straße 61, 01187 Dresden, Germany*
[3]*Collaborative Innovation Center of Advanced Microstructures, Nanjing University, 210093 Nanjing, P. R. China*
[4]*Center for Advancing Electronics Dresden – cfaed, TU Dresden, 01062 Dresden, Germany*

(Received 8 August 2017; revised manuscript received 31 May 2018; published 4 September 2018)

We investigate here the asymmetric domain-wall conductivity (DWC) of neighboring domain walls (DWs) in *z*-cut periodically poled $LiNbO_3$ single crystals. Asymmetric domain-wall conductivity is observed by scanning-probe-microscopy-based methods and the DW inclination α is measured by Cherenkov second-harmonic-generation microscopy. A generalizable dipole-tunneling current model is proposed to elucidate the phenomenon, which also accounts for DW roughness. Our research provides a valuable perspective on how to influence DWC on the microscopic and macroscopic length scales, and the required nanoscopic insights.

DOI: 10.1103/PhysRevApplied.10.034002

I. INTRODUCTION

It is well-known that the distribution and characteristics of ferroelectric domains are important for the application of ferroelectric materials in nonlinear optics, photovoltaics, electro-optics, and memory devices [1]. Recently, however, interesting electronic properties have been revealed for domain walls (DW) in many ferroic materials [1], in strong contrast to the characteristics of extended domains. In fact, it is 10 years since the report on domain-wall conductivity (DWC) by Gainutdinov *et al*. [2], in which the authors apply conductive atomic force microscopy (cAFM) to probe DWs in $C_6H_{17}N_3O_{10}S$. The palette of prospective DWC materials since then has been extended to $BiFeO_3$ [3–8], $LiNbO_3$ [9,10], $Pb(Zr_{0.2}Ti_{0.8})O_3$ [11], $REMnO_3$ [12–16,35] with RE = Y, Er, Tb, Ho, and others [17]. Notably, the formation of ferroelectric domains can be reproducibly controlled at the microscopic length scale [18–20], while the DW conductivity may be elegantly tuned through DW doping [9,21], offering huge potential for prospective applications of DWC in nanoscale devices, such as nonvolatile memory, logic elements, and local-strain sensors [1,20].

Nevertheless, DWC is a complex phenomenon that is strongly dependent on intrinsic material properties. For instance, DWs are not uniquely conductive in any material A or B per se, but may exhibit clear differences in the two materials [1]. Moreover, DWC in the same material might also vary dramatically between metallic- and fully-insulating-like properties [4,12], as already shown in the seminal work by Seidel *et al*. [5]. Discussions on the origin of DWC thus become very diverse, including theories that assume a nonzero component of polarization that stands perpendicular to the Bloch- or Néel-type DW to be the driving potential for DWC [5]. Other work relates DWC to the electronic band bending near the DW [5,14] or postulates DWC to be a combination of Schottky emission and space-charge currents [6,22]. Most work, however, considers DWC to result from free-charge-carrier hopping along head-to-head and tail-to-tail DWs [1,9,12,14,23–25].

In the present work, we explore the subject of DWC in a periodically poled, non-doped congruent *z*-cut $LiNbO_3$ single crystal, with DWs being arranged parallel to each other while having a wall-to-wall separation of approximately 5 μm. The sample is chemically and mechanically polished to a thickness of 73 μm, revealing a surface root-mean-square roughness of <30 nm. As detailed below, we observe a strong difference in the conductivity of neighboring DWs, which are found to be head-to-head and tail-to-tail, respectively. Furthermore, the DW roughness is found to have a strong influence of on DWC, when comparing cAFM data with piezoresponse force microscopy (PFM) measurements. Since all DWs are inclined by an average angle $\bar{\alpha} = 0.37^\circ$ with respect to the *z* axes [as checked by 3D Cherenkov second-harmonic-generation (CSHG) microscopy] [26], we are able to simulate DWC as an elementary tunneling process of electrons along the charged DWs. This provides a potential way to explain the samples' *p*- and *n*-type transport characteristics.

*lukas.eng@tu-dresden.de

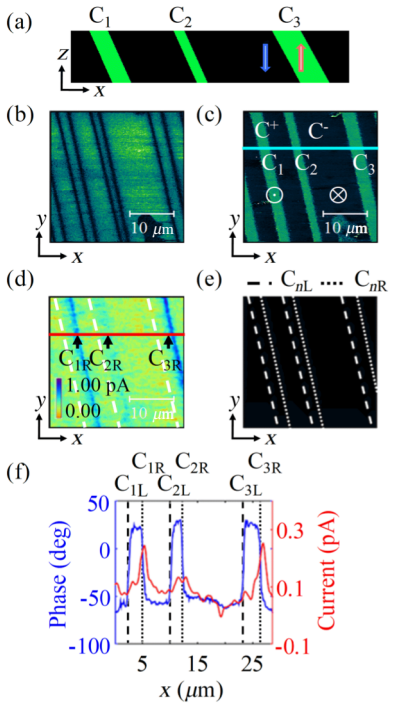

FIG. 1. (a) Schematic arrangement of head-to-head and tail-to-tail DWs in periodically poled $LiNbO_3$ single crystals. All DWs are parallel to each other and inclined with respect to the z axes; (b) PFM amplitude, (c) PFM phase, and (d) cAFM images over a $30 \times 30\ \mu m^2$ sample area of the periodically poled $LiNbO_3$ single crystal. Note the different current densities flowing in C_R and C_L DWs, as schematically depicted in (e) and also in the cross section (f). Larger currents flow at head-to-head DWs C_{1R}, C_{2R}, and C_{3R}.

II. EXPERIMENTAL PHENOMENON

Figure 1(a) sketches the $LiNbO_3$ single-crystalline sample that exhibits a set of periodically poled domains. Note that neighboring domain walls remain parallel to each other into the crystal bulk, but are appreciably inclined with respect to the z axes, hence alternately forming head-to-head and tail-to-tail DWs.

Figures 1(b) and 1(c) show the PFM amplitude and phase images recorded over a $30 \times 30\ \mu m^2$ scan area (PFM parameters are 300 kHz and 100 mV amplitude). The PFM amplitude in Fig. 1(b) stays consistent overall, beyond the defect site located at the bottom of the image, and at the DWs. The PFM phase Fig. 1(c) clearly distinguishes C^+ from C^- domains, colored in green and black for polarization vectors pointing up (out-of-plane) and down (into-the-plane), respectively. We denote three C^+ domains C_1, C_2, and C_3, along the blue line in Fig. 1(c), that all possess two different interfaces right (R) and left (L) to the neighboring C^- domain, i.e., C_{1R}, C_{2R}, and C_{3R} are head-to-head DWs to the right of every C^+ domain, while C_{1L}, C_{2L}, and C_{3L} are tail-to-tail DWs facing to the left of every such C^+ domain, respectively.

In Fig. 1(d), we display the DW current as recorded by cAFM in a backward scan direction applying a -10 V bias to the samples' bottom electrode. A larger DW current of up to 1 pA (colored blue) is always recorded at C_R interfaces, with the current at the C_{2R} DW showing a slightly lower value, most probably due to lower DW inclination.

Figure 1(e) summarizes the DWC findings by associating dotted and dashed lines to the C_R and C_L DW interfaces that exhibit a high and low DWC at the -10 V bias voltage, respectively. It becomes even clearer that neighboring DWs have asymmetric conductivity, when inspecting the cross section in Fig. 1(f) that superposes the PFM phase and DW current data taken along the blue and red lines marked in Figs. 1(c) and 1(d), respectively. Figure 1(f) clearly displays that the larger DWC always coincides with the C_R interface of C^+ domains. Moreover, we reproduce these findings in three different ways: (i) inspecting the same sample by cAFM and PFM using two different SPM machines; (ii) comparing both trace and retrace for all these measurements; and (iii) using both full-metal Pt and Pt-coated Si tips for AFM inspection. All these results are fully congruent and support the graphs plotted in Fig. 1 (see Section A in the Supplemental Material [27] for details).

Previously, the arrangement and inclination of head-to-head and tail-to-tail DWs as sketched in Fig. 1(a) was purely hypothetical. This setting of periodically poled DWs is proved by applying a 3D reconstruction of DW inclination angles using CSHG microscopy (for CSHG details see [26]) over a large area that includes also the area of Figs. 1(b–d) [blue square in Fig. 2(a)], located near irregularly shaped domains in the upper part of Fig. 2(a). DWs appear reddish in this $90 \times 90\ \mu m^2$ CSHG plot that is recorded close to the sample surface (at a z-height value of $\sim 70\ \mu m$; zero reference at the sample bottom).

Figure 2(b) displays an x-z cross section taken from 73 to 13 μm into the depth of our sample along the yellow line as indicated in Fig. 2(a). We clearly see most DWs to be aligned parallel to each other, however, being tilted off the sample normal (z axes) by an angle α varying in the range 0.25°–1°, with an average angle $\bar{\alpha} = 0.37°$. Figure 2(b) not only proves that all DWs are severely inclined with respect to the sample normal and thus are all good candidates for DWC, but equally well confirms that the C_{1R}, C_{2R}, and C_{3R} interfaces indeed constitute head-to-head DWs, while the C_{1L}, C_{2L}, and C_{3L} boundaries are of the tail-to-tail type.

Figure 2(c) illustrates the CSHG 3D view of DWs taken over a lateral scan range of $130 \times 130\ \mu m^2$ and across the full sample thickness of 73 μm. The white square signifies the area of Fig. 2(a). Notably, all DWs analyzed here for DWC are "through domains," i.e., DWs that fully penetrate across the whole $LiNbO_3$-single-crystal thickness and hence connect the top with the bottom sample surface.

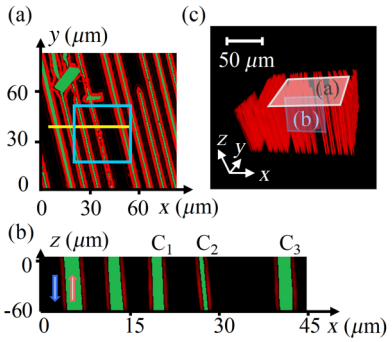

FIG. 2. (a) Periodically poled $LiNbO_3$ domain structure detected by CSHG over a 90×90 μm^2 scan close to the sample surface at $z = 73$ μm. The green square shows the measurements performed by SPM in Fig. 1; (b) CSHG x-z cross section recorded 60 μm into the depth of the PPLN sample along the yellow line indicated in (a). Note that all DWs are inclined with respect to the z axes by an average angle $\bar{\alpha} = 0.37°$; (c) CSHG 3D view across the whole periodically poled $LiNbO_3$ sample over a 130×130 μm^2 area. Note that all DWs are through domains. The white square and the blue square correlate with (a) and (b), respectively.

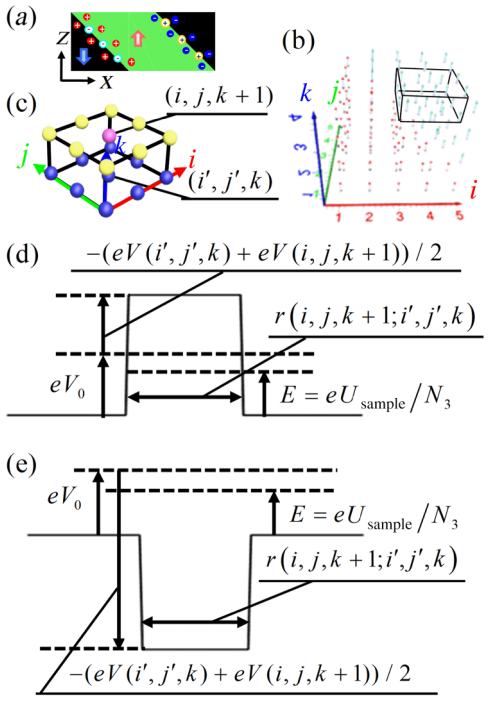

FIG. 3. (a) Sketch of a single C^+ domain facing a head-to-head (C_R) and a tail-to-tail (C_L) DW to the right and left neighboring C^- domains, respectively. Both DWs are assumed to be fully planar and straight, but inclined to the z axes. Positive and negative bound charges (orange and green circles) at head-to-head and tail-to-tail DWs are compensated by mobile electrons and holes (blue and red solid spheres), respectively. (b) Magnification of the schematic arrangement of electrical dipole moments, as used in our tunneling transport model. Green and purple arrows depict up and down polarization vectors, respectively. PFM (Fig. 1) and CSHG (Fig. 2) data serve as input here. (c) Sketch of a single mesh for modeling. The tunneling current flowing across point $(i,j,k+1)$ (shown in pink) is calculated by averaging the current from the adjacent layer in the z direction $(i',j',k)\{i' \in \{i-1, i, i+1\}, j' \in \{j-1, j, j+1\}\}$ (shown in blue). Sketches of the (d) barrier-tunneling and (e) well-tunneling processes for electrons.

III. DIPOLE-TUNNELING MODEL SIMULATION

The overall situation is summarized in Fig. 3(a) which shows a sketch of an inclined C^+ domain that is separated by a head-to-head (C_R) and a tail-to-tail (C_L) DW to the right and left neighboring C^+ domain, respectively. For simplicity, we firstly assume these two "180° DWs" to be planar and smooth, thus possessing a DW roughness of exactly zero. Red and blue arrows indicate the direction of spontaneous polarization in the C^+ and C^- domains, respectively.

Now, head-to-head and tail-to-tail DWs carry positive and negative bound charges, as marked in Fig. 3(a) with orange and blue circles, respectively. Therefore, these bound charges may attract free charge carriers of opposite sign in order to compensate for the large electrical field emerging from the bound charge density. As a result, free holes and free electrons [shown as red and dark blue solid spheres in Fig. 3(a)] gather around the tail-to-tail and head-to-head DWs; note that this compensation mechanism again is material dependent, with free charges stemming either from within the ferroelectric crystal (internal compensation) or being injected externally through the sample surfaces. It is these free charge carriers that then contribute to the measured DWC along DWs. Moreover, the free charge carriers are also responsible for both the DWC selectivity observed between C_R and C_L DWs, and the DWC dependence on domain-wall roughness, as discussed later.

We are interested in understanding the DWC behavior from an atomistic point of view. Therefore, we introduce here a quantum-mechanical model that treats DWC as a tunneling process [20,28,29] along head-to-head and tail-to-tail DWs. What we need as inputs are: (i) the applied electrical potential; (ii) the charge-carrier concentration; (iii) a surface up/down-polarization distribution as governed by Fig. 1(c); as well as (iv) the domain wall inclination (Fig. 2). All these parameters are introduced as dimensionless in order not to complicate the calculations. Also, our simulation is scale invariant and can be adopted to other length-scale scenarios. We expect a twofold benefit from these simulations: first, our calculation should deliver a qualitatively similar behavior of DWC as experimentally mapped in Fig. 1(d), while second a clear distinction between head-to-head and tail-to-tail DWs is anticipated that then can be directly associated to n- and p-type conduction [6,9,23].

The tunneling scenario is split into two subproblems which are (A) the sample and (B) the tip-sample modeling. While (A) accounts for the charge-carrier transport across the sample calculated layer-by-layer in the z direction starting from the sample bottom to its top, the tip-scenario (B) accounts for tunneling processes between the sample top surface and the effective tip apex. The potential of -10 V is applied to the sample bottom surface while the tip is grounded.

A. Tunneling in the sample

1. Setup of the model

The sample problem (A) is sectioned into a regular grid of $256 \times 256 \times 36$ points along the x, y, and z directions, respectively. In our model, we assume a dielectric dipole with the dipole moment $\vec{p}(i,j,k)$ to be located at the center of any such point (i,j,k), with $\{i,j,k \in N | 1 \le i,j \le 256, 1 \le k \le 36\}$. The dipoles' magnitude is given by the product of spontaneous polarization P_s of the material (here $LiNbO_3$) and the grid volume $dv = \Delta x \Delta y \Delta z$, i.e., $\vec{p}(i,j,k) = P_s \hat{P}(i,j,k)\, dv$, while its orientation is determined from both the initial PFM data in Fig. 1(c) revealing the surface polarization orientation at $z = 73$ μm, and the CSHG data (Fig. 2) that allows the interpolation of the domain wall inclined by 0.37° into the bulk, namely $\hat{P}(i,j,k) = \hat{P}(\lfloor i - (36-k)\tan(0.37^\circ) \rfloor, j, 36)$. The simulation is calculated in a size 1000 times smaller than the experiment due to the limit of calculation. Note, again, that here we assume the DWs to be completely straight and have no roughness at all. Figure 3(b) sketches this arrangement of dipoles, displayed for better visibility, with many fewer grid points ($5 \times 5 \times 4$ points only) and with a larger DW inclination angle of 45°.

2. Electric-potential distribution

The electric potential at each grid point V(i,j,k) is calculated by the sum of the contributions from surrounding dipoles V_d(i,j,k) (including image dipoles that mimic the bottom electrode) and the contributions from surface screening charges V_s(i,j,k).

The dipole contribution V_d(i,j,k) in grid point (i,j,k) $\{i,j,k \in N | 1 \le i,j \le 256, 1 \le k \le 36\}$ is calculated by adding up the contributions from surrounding dipoles:

$$\vec{p}(i',j',k') \quad \{i - \Delta n \le i' \le i + \Delta n, j - \Delta n \le j' \le j + \Delta n, k - \Delta n \le k' \le k + \Delta n | (i',j',k') \ne (i,j,k)\},$$

i.e.,

$$V_d(i,j,k) = \sum_{(i',j',k') \ne (i,j,k)} \frac{1}{4\pi\varepsilon_0} \frac{\vec{p}(i',j',k') \cdot \hat{r}(i',j',k';i,j,k)}{r^2(i',j',k';i,j,k)}. \tag{1}$$

Since we have a bottom electrode connected to the sample, an image method is used to achieve an identical potential distribution throughout the bottom of the sample, i.e., we put imaged dipoles of grid points above $k = 1$ below them.

The screening effect on the top surface is modeled by a layer of screening charges $Q_s(i,j,37) = -\theta Q_{sb}(i,j,36)$ placed just above the top layer ($k = 36$), where θ is the screening coefficient and $Q_{sb}(i,j,36) = \vec{P}_z(i,j,36) \cdot \vec{S}_{\text{grid}}$ is the surface bound charge of the grid point (i,j,36) on the top layer, with $\vec{S}_{\text{grid}}$ representing the surface element of a grid point. These surface screening charges contribute to the electric potential as

$$V_s(i,j,k) = \frac{1}{4\pi\varepsilon_0} \frac{Q_s(i',j',37)}{r(i',j',37;i,j,k)}. \tag{2}$$

3. Bound charge distribution and charge-carrier distribution

We derive the bound charge distribution by Poisson's equation:

$$\begin{aligned} Q_b(i,j,k) &= -\varepsilon_0(\nabla^2 V)dv \\ &= -\varepsilon_0 \Delta x \Delta y \Delta z \\ &\quad \left\{ \frac{V(i+1,j,k) + V(i-1,j,k) - 2V(i,j,k)}{\Delta x^2}\bigg|_{y,z} \right. \\ &\quad + \frac{V(i,j+1,k) + V(i,j-1,k) - 2V(i,j,k)}{\Delta y^2}\bigg|_{z,x} \\ &\quad \left. + \frac{V(i,j,k+1) + V(i,j,k-1) - 2V(i,j,k)}{\Delta z^2}\bigg|_{x,y} \right\}. \end{aligned} \tag{3}$$

We assume the interaction between bound and mobile screening charges to decay exponentially, very similar to the Debye screening length. The electron and hole charges close to every grid point then can be expressed as

$$\begin{aligned} Q_e(i,j,k) &= -c_e \sum_{\{i',j',k'\}} \frac{\gamma_e^2}{8\pi} Q_b(i',j',k') e^{-\gamma_e \cdot r(i',j',k';i,j,k)}\Big|_{Q_b(i',j',k')>0}, \\ Q_h(i,j,k) &= -c_h \sum_{\{i',j',k'\}} \frac{\gamma_h^2}{8\pi} Q_b(i',j',k') e^{-\gamma_h \cdot r(i',j',k';i,j,k)}\Big|_{Q_b(i',j',k')<0}, s \end{aligned} \tag{4}$$

where $c_{e/h}$ and $\gamma_{e/h}$ are the screening and charge distribution coefficients for electrons and holes, respectively, with e standing for electrons and h standing for holes. For ideal

cases, bound charges are fully screened by free charge carriers, $c_e = c_h = 1$. Notably, $\gamma_e > \gamma_h$ for n-type materials, while $\gamma_e < \gamma_h$ for p-type materials. A series of $\gamma_{e/h}$ ranging from 0.2 to 5.0 are examined for the simulation. As is expected, the exact value of $\gamma_{e/h}$ influences the shape and height of current peaks, e.g., larger $\gamma_{e/h}$ corresponds to higher current peaks, but it does not change the result about which side of DWs (C_L or C_R) conducts better. For the following discussion, $\gamma_e = 5.0$ and $\gamma_h = 4.7$ are chosen for n-type cases while the inverted set are applied to p-type cases.

4. Tunneling current in the sample

The transmitted current is calculated layer-by-layer from the bottom to the top surface. Considering a single "unit cell" [see the enlarged view in Fig. 3(c)] around an arbitrary point $(i,j,k+1)$ $(2 \le i,j \le 255, 1 \le k \le 35, i \in N, j \in N, k \in N)$ depicted as a pink ball in Fig. 3(c), the current flux into point $(i,j,k+1)$ is calculated by averaging the current (including electron and hole currents) from the neighboring grid points (i',j',k) [blue balls in Fig. 3(c)] in the downward layer (layer k). Hence,

$$I_{e/h}(i,j,k+1) = \frac{1}{9} \sum_{i'=\{i-1,i,i+1\},j'=\{i-1,j,j+1\}} \times I_{e/h}(i,j,k+1;i',j',k). \quad (5)$$

The tunneling current from (i',j',k) to $(i,j,k+1)$ is calculated by

$$I_{e/h}(i,j,k+1;i',j',k) = |Q_{e/h}(i',j',k)| \cdot T_{e/h}(i,j,k+1;i',j',k) \cdot I_{e/h}(i',j',k), \quad (6)$$

where $T_{e/h}(i,j,k+1;i',j',k)$ is the transmission probability of electrons and holes, respectively, from grid point (i',j',k) to grid point $(i,j,k+1)$, which is calculated as shown below, with an intrinsic potential barrier eV_0 assumed for all tunneling process.

(a) Transmission probability for electrons.

For electrons, we consider the potential barrier (or well) height for an electron to move from point (i',j',k) to point $(i,j,k+1)$ as the sum of intrinsic potential barrier and the average of potential energy on these two points, i.e., $(eV_0 - eV_{ave})$, where $V_{ave} = (eV(i',j',k) + eV(i,j,k+1))/2$ represents the average potential between the grid points. The initial energy of the electron is taken as $E = eU_{sample}/N_3$ (U_{sample} is the voltage applied to the sample, N_3 is the number of layers in the z direction).

If the initial energy of the electron is lower than the height of potential barrier or well, then the process should be a tunneling process through a potential barrier. On the contrary, when the initial energy is higher, then the electron tunnels through the potential well.

For potential barriers [as shown in Fig. 3(d)], the transmission probability is

$$T_e(i,j,k+1;i',j',k) = \exp\left(-2r(i,j,k+1;i',j',k) \times \sqrt{\frac{2m_e}{\hbar^2}(eV_0 - eV_{ave} - E)}\right), \quad (7)$$

where m_e is the mass of an electron, $\hbar$ is the reduced Planck constant, and $r(i,j,k+1;i',j',k)$ is the distance from source grid point (i',j',k) to the target grid point $(i,j,k+1)$.

For potential wells [as shown in Fig. 3(e)], the transmission probability can be expressed as

$$T_e(i,j,k+1;i',j',k) = \frac{4K_1^2K_2^2}{(K_1^2+K_2^2)^2\sin^2(\theta) + 4K_1^2K_2^2\cos^2(\theta)}, \quad (8)$$

where $K_1 \triangleq \sqrt{2m_e/\hbar^2}$, $K_2 \triangleq \sqrt{2m_e[E + eV_0 - eV_{ave}]/\hbar^2}$, and $\theta \triangleq 2K_2 \cdot r(i,j,k+1;i',j',k)$.

(b) Transmission probability for holes.

Similarly, the same works for holes. We define potential barrier or well height as $(eV_0 + eV_{ave})$. The initial energy of a hole is $E = eU_{sample}/N_3$.

For a potential barrier, the transmission probability is

$$T_h(i,j,k+1;i',j',k) = \exp\left(-2r(i,j,k+1;i',j',k) \times \sqrt{\frac{2m_h}{\hbar^2}(eV_0 + eV_{ave} - E)}\right), \quad (9)$$

where m_h is the mass of hole.

For a potential well, the transmission probability is

$$T_h(i,j,k+1;i',j',k) = \frac{4K_1^2K_2^2}{(K_1^2+K_2^2)^2\sin^2(\theta) + 4K_1^2K_2^2\cos^2(\theta)}, \quad (10)$$

where $K_1 \triangleq \sqrt{2m_h/\hbar^2}$, $K_2 \triangleq \sqrt{2m_h(E + eV_0 + eV_{ave})/\hbar^2}$, and $\theta \triangleq 2K_2 \cdot r(i,j,k+1;i',j',k)$.

B. Tunneling from top layer to the tip

The tunneling current flux between the sample top surface and tip (B) is treated in a similar fashion to the sample problem (A), as we calculate the tunneling current from every grid point on the upper surface $(i,j,36)$ $\{i,j \in N | 2 \leq i,j \leq 255\}$ to an imagined grid point (the tip) just above it $(i,j,37)$; however, the tip is kept at ground potential, i.e., $V(i,j,37) \triangleq U_{\text{tip}} = 0$. Similar to the process inside the crystal, an intrinsic potential barrier eV_1 is set up between the top layer and the tip, except that $V_1 > V_0$. From the sum of the current contributions of both electrons and holes, i.e., $I(i,j,37) = I_e(i,j,37) + I_h(i,j,37)$, we obtain the simulated current map [Figs. 2(d) and 2(e)] that is then directly compared to the experimental findings of Fig. 1(d). Noting that, this model can in principle be widely applied to ferroelectric materials, irrespective of crystal systems and domain structures.

IV. DISCUSSION

Figures 4(a) and 4(b) illustrate the x-y current maps when assuming the $LiNbO_3$ material to be n or p type, respectively. These two images clearly show very different features, with larger currents flowing along head-to-head and tail-to-tail DWs for n- and p-type host materials, respectively. Again, we compare the two results by using cross sections [Fig. 4(c)] that are taken at the same position as for Fig. 1(d) [red and yellow line in Figs. 4(a) and 4(b)] and overlaid here with the polarization data (shown in blue). As seen in Fig. 4(c), the simulated current cross section for an n-type material shows two large peaks close to the C_{1R} and C_{3R} DWs, and a slightly reduced peak near the C_{2R} DW, agreeing well with the experimental results shown in Fig. 1(d). Conversely, the simulations for a p-type host material result in current peaks near C_L DWs (tail-to-tail). We conclude that the conductivity of our DWs shown in Fig. 1 corresponds to the n-type transport mechanism.

Note that the selective conductivity, i.e., which DW conducts better, is in fact determined by both the type of the DW (tail-to-tail or head-to-head) and the charge-carrier type in the bulk, while the magnitude of the DW current can be modified by the tip-sample barrier V_1. When the tip-sample barrier is low, the magnitude of the current peak slightly fluctuates but stays broadly at the same level. This means that, for the conditions we used in this paper (the tip resistance is low and the sample surface is dry and clean), a certain amount of fluctuation of the tip-sample barrier will not greatly affect the detection of DW current. With further increases of the tip-sample barrier, the magnitude of the current peak decreases sharply. Therefore, if the conductive coating of the tip is damaged, or there is undesirable contact between the tip and the sample, or there is extremely low environmental humidity, DW current would be hardly detectable due to the limited resolution of the instruments.

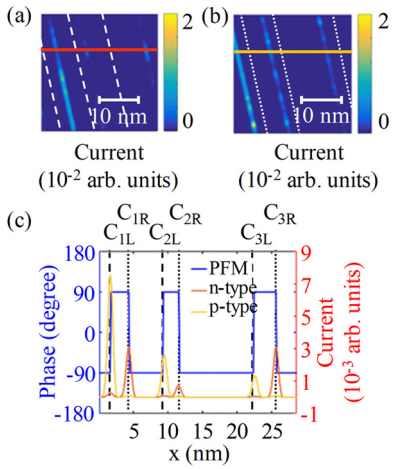

FIG. 4. Simulated current distribution for n-type (a) and p-type (b) $LiNbO_3$ material. Note again that positions C_R and C_L DWs are marked by white dotted and dashed lines; (c) cross section along the red line in (a) and the yellow line in (b), including also the PFM phase data from Fig. 1(c). The larger currents at head-to-head walls indicate the n-type PPLN sample behavior.

In this model, material-related parameters are spontaneous polarization, domain structures, and the charge-carrier concentration. Given these parameters, the model could in principle be extended to broader ferroelectric materials, thus helping to predict DWC in different materials and to anticipate the properties of future nanodevices.

V. MODEL EXTENDED FOR DOMAIN-WALL ROUGHNESS

We now extend our tunneling model by also accounting for the DW roughness, as experimentally observed both in the PFM and CSHG data. DW roughness may be heavily affected by both the local disorder and cooperative long-range dipolar interactions [30]. In our present case for DWC in periodically poled lithium niobate (PPLN), DW roughness may show up in both an in-plane roughening (x-y plane) (similar to the one in [31]) and an out-of-plane roughening (x-z plane). Of interest here is how the latter impacts DWC. Note that the inclined DW per se induces local potential fluctuations that then compete with flattening effects to straighten the DW. Both the CSHG [26] and recent TEM results [32] for $LiNbO_3$ clearly underline that even noninclined nominally flat DWs possess a minimal roughness of approximately 7 unit cells at room temperature.

Figures 5(a) and 5(b) schematically display the modeling scenario for the flat and rough DW, respectively, assuming that the polarization dipole distributed along our rough DW may jump by one mesh size compared with the smooth DW. The simulated current for rough DWs is

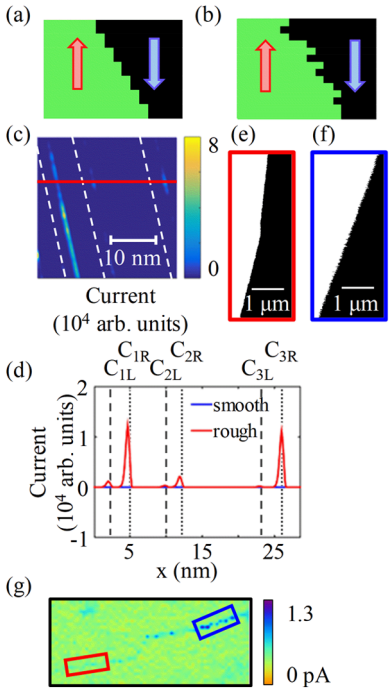

FIG. 5. Sketches for a smooth (a) and rough (b) DW, as adopted for our QM tunneling model. (c) Simulated current distribution for the rough DWs, with current peaks arising almost at the same positions as for the smooth DWs [see Fig. 4(a)] but with a current six orders of magnitude larger. C_L DWs are marked with white dashed lines. (d) Cross section taken along the red line in (c) [i.e., the same profile as for Figs. 4(a) and 5(c)] displaying the DWC for smooth (blue) and rough DWs (red). DW roughness dramatically increases the DWC along head-to-head DWs in the periodically poled $LiNbO_3$ sample. (e), (f) PFM phase images of different parts of a DW in an ultraviolet-laser-induced polarized Mg-doped $LiNbO_3$ sample with DW roughness presented by correlation function B for a space step of 20 nm as 80 nm^2 in (e) and 980 nm^2 in (f), respectively. (g) cAFM image with the red square corresponding to (e) and blue square corresponding to (f), while the DWC is higher in the blue square.

shown in Fig. 5(c), with the high and low conductivity plotted in yellow and blue. The cross section in Fig. 5(d) coincides well with Figs. 1(f) and 4(c). Note that highly conductive areas for the rough DW case still coincide with C_R or head-to-head DWs. Also, the roughened DW has a DWC that is six orders of magnitude larger [red line in Fig. 5(d)] than the DWC along the straight DW [blue line in Fig. 5(d)]. At that scaling of Fig. 5(d), three peaks in the simulated current for rough DWs can be observed, while the simulated current for smooth DWs is almost invisible.

Experiments are also done to confirm the influence of DW roughness on DWC. A large ferroelectric domain possessing a long DW with variable in-plane DW roughness at different parts is polarized by a ultraviolet-laser-induced polarization method [10] in a Mg-doped $LiNbO_3$ single crystal. As we apply DW roughness to two nearby DWs [Figs. 5(e) and 5(f)] with $\Delta q = 20$ nm being the 2-pixel distance deduced from our PFM images [31–34], we find that the DW roughness is higher in Fig. 5(f) (980 nm^2) than in Fig. 5(e) (80 nm^2). The DW roughness is calculated by the formula

$$B(\Delta q) = \overline{\langle |u(q+\Delta q) - u(q)|^2 \rangle}, \tag{11}$$

where $u(q)$ is the transverse displacement at longitudinal coordinate q along the wall and $\langle \cdots \rangle$ and $\overline{\cdots}$ denote disorder and thermal averages, respectively.

The cAFM test [Fig. 5(g)] indicates that the DW with higher roughness in the blue square [corresponding to the area of Fig. 5(f)] does indeed show higher conductivity, possessing DW current of about 1.3 pA, compared with the DW with lower roughness in the red square [corresponding to the area of Fig. 5(e)], with its DW current at the noise level.

In fact, DW roughness in Figs. 5(e) and 5(f) is calculated for various Δq ranging from 10 to 156 nm. Although DW roughness is related to Δq, we find that the selection of Δq does not change our judgment about the DW roughness comparison, i.e., the DW in Fig. 5(f) is rougher than that in Fig. 5(e), which is regarded as resulting from the inhomogeneous and anisotropic properties in the sample [33] and the fluctuations of poling conditions [32]. Since DW roughness can be adjusted by changing the scan direction [33] or the scan rate while polarizing the domain with the PFM tip, as we demonstrate in the supplementary materials (part B) [27], it is very likely that we will eventually be able to manually control DWC by adjusting DW roughness, thus dramatically improving the application potential of DWC.

Note that both in-plane [33] and out-of-plane DW roughness [32] exist in $LiNbO_3$ due to its significant anisotropic properties. Since the DW growth in $LiNbO_3$ single crystals has preferred directions [33], they are more likely to be smooth if they are generated along these directions; otherwise, they will form a zig-zag shape including tiny sections aligning in the preferred directions, thus possessing higher DW roughness. Considering that in-plane DW roughness is closely related to out-of-plane DW roughness, the DWCs in Fig. 5(g) also reflect the impact of out-of-plane DW roughness, which has already been presented in the tunneling simulation.

VI. CONCLUSION

In conclusion, we report on the conductive behavior of ferroelectric DWs in $LiNbO_3$ single crystals. After 3D analysis of CSHG, asymmetric conductivity in the seemingly equal 180° parallel DWs detected by cAFM can be considered as a result of the transport difference between head-to-head and tail-to-tail polarization configurations in *n*-type materials. As backed up by a

dipole-tunneling model, the DWC can be viewed as a quantum-mechanical tunneling process along the DWs. In the present setup, head-to-head DWs promoting electron transport are favored, corresponding well with the cAFM experiment.

This model has only three material-related input parameters (spontaneous polarization, domain structures, charge-carrier concentration), and the simulated DW current can be vividly displayed in the same way as the cAFM experiment. Using this model, DWC can be predicted before any complicated domain configurations are actually fabricated in certain materials, thus making the material selection and structural design for nanodevices based on DWC more efficient.

In addition, the DW roughness plays an essential role in deciphering the magnitude of DW current readable from a single wall. This provides another controllable degree of freedom on domain-wall conduction, i.e., manipulating domain-wall conduction by changing domain-wall roughness using different polarization methods and subsequent treatment [27]. In this way, the sensitivity of on/off states for DWC could be modulated, when it is used as memory or switching devices. Moreover, taking DW roughness and applied field as two inputs, e.g. smooth/rough DWs and light (electric bias) on/off, DWC could be considered as output signal of double-channel and multi-state logic elements.

ACKNOWLEDGMENTS

We would like to thank P. Paruch for helpful discussions. Financial support by the National Key Research Program of China (Grant No. 2016YFA0201004), the 973 Project of MOST (Grant No. 2015CB921201), the National Natural Science Foundation of China (Grants No. 51672123 and 61671235), the Deutsche Forschungsgemeinschaft (DFG) within the cluster of excellence (Center for Advancing Electronics Dresden, cfaed) and the research grant HA 6982/1-1 is gratefully acknowledged. S.X. acknowledges the support by China Scholarship Council and Deutsche Forschungsgemeinschaft.

[1] G. Catalan, J. Seidel, R. Ramesh, and J. F. Scott, Domain wall nanoelectronics, Rev. Mod. Phys. **84**, 119 (2012).

[2] R. V. Gainutdinov, N. V. Belugina, A. L. Tolstikhina, and O. A. Lysova, Criterion for identification of ferroelectric domains in TGS crystals from AFM images, Crystallogr. Rep. **52**, 332 (2007).

[3] I. Stolichnov, M. Iwanowska, E. Colla, B. Ziegler, I. Gaponenko, P. Paruch, M. Huijiben, G. Rijnders, and N. Setter, Persistent conductive footprints of 109° domain walls in bismuth ferrite films, Appl. Phys. Lett. **104**, 132902 (2014).

[4] Y.-P. Chiu, Y.-T. Chen, B.-C. Huang, M.-C. Shih, J.-C. Yang, Q. He, C.-W. Liang, J. Seidel, Y.-C. Chen, R. Ramesh, and Y.-H. Chu, Atomic-scale evolution of local electronic structure across multiferroic domain walls, Adv. Mater. **23**, 1530 (2011).

[5] J. Seidel, L. W. Martin, Q. He, Q. Zhan, Y.-H. Chu, A. Rother, M. E. Hawkridge, P. Maksymovych, P. Yu, M. Gajek, N. Balke, S. V. Kalinin, S. Gemming, F. Wang, G. Catalan, J. F. Scott, and N. A. Spaldin, J. Orenstein, and R. Ramesh, Conduction at domain walls in oxide multiferroics, Nat. Mater. **8**, 229 (2009).

[6] S. Farokhipoor and B. Noheda, Conduction Through 71° Domain Walls in $BiFeO_3$ Thin Films, Phys. Rev. Lett. **107**, 127601 (2011).

[7] P. Maksymovych, J. Seidel, Y.-H. Chu, P. Wu, A. P. Baddorf, L. Q. Chen, S. V. Kalinin, and R. Ramesh, Dynamic conductivity of ferroelectric domain walls in $BiFeO_3$, Nano Lett. **11**, 1906 (2011).

[8] A. Rana, H. Lu, K. Bogle, Q. Zhang, R. Vasudevan, V. Thakare, A. Gruverman, S. Ogale, and N. Valanoor, scaling behavior of resistive switching in epitaxial bismuth ferrite heterostructures, Adv. Funct. Mater. **24**, 3962 (2014).

[9] M. Schröder, A. Haußmann, A. Thiessen, E. Soergel, T. Woike, and L. M. Eng, Conducting domain walls in lithium niobate single crystals, Adv. Funct. Mater. **22**, 3936 (2012).

[10] C. Godau, T. Kämpfe, A. Thiessen, L. M. Eng, and A. Haußmann, Enhancing the domain wall conductivity in lithium niobate single crystals, ACS Nano **11**, 4816 (2017).

[11] J. Guyonnet, I. Gaponenko, S. Gariglio, and P. Paruch, Conduction at domain walls in insulating $Pb(Zr_{0.2}Ti_{0.8})O_3$ thin films, Adv. Mater. **23**, 5377 (2011).

[12] D. Meier, J. Seidel, A. Cano, K. Delaney, Y. Kumagai, M. Mostovoy, N. A. Spaldin, R. Ramesh, and M. Fiebig, Anisotropic conductance at improper ferroelectric domain walls, Nat. Mater. **11**, 284 (2012).

[13] D. J. Kim, J. G. Connell, S. S. A. Seo, and A. Gruverman, Domain wall conductivity in semiconducting hexagonal ferroelectric $TbMnO_3$ thin films, Nanotechnology **27**, 155705 (2016).

[14] W. Wu, Y. Horibe, N. Lee, S. W. Cheong, and J. R. Guest, Conduction of Topologically Protected Charged Ferroelectric Domain Walls, Phys. Rev. Lett. **108**, 077203 (2012).

[15] T. Choi, Y. Horibe, H. T. Yi, Y. J. Choi, W. Wu, and S. W. Cheong, Insulating interlocked ferroelectric and structural antiphase domain walls in multiferroic $YMnO_3$, Nat. Mater. **9**, 253 (2010).

[16] J. A. Mundy, J. Schaab, Y. Kumagai, A. Cano, M. Stengel, I. P. Krug, D. M. Gottlob, H. Doganay, M. E. Holtz, R. Held, Z. Yan, E. Bourret, C. M. Schneider, D. G. Schlom, D. A. Muller, R. Ramesh, N. A. Spaldin, and D. Meier, Functional electronic inversion layers at ferroelectric domain walls, Nat. Mater. **16**, 622 (2017).

[17] Y. Kim, M. Alexe, and E. K. H. Salje, Domain wall conductivity in semiconducting hexagonal ferroelectric $TbMnO_3$ thin films, Appl. Phys. Lett. **96**, 032904 (2010).

[18] L. M. Eng, M. Bammerlin, Ch. Loppacher, M. Guggisberg, R. Bennewitz, R. Lüthi, E. Meyer, Th. Huser, H. Heinzelmann, and H.-J. Güntherodt, Ferroelectric

domain characterisation and manipulation: A challenge for scanning probe microscopy, Ferroelectrics **222**, 153 (1999).

[19] N. Balke, S. Choudhury, S. Jesse, M. Huijben, Y.-H. Chu, A. P. Baddorf, L. Q. Chen, R. Ramesh, and S. V. Kalinin, Deterministic control of ferroelastic switching in multiferroic materials, Nat. Nanotechnol. **4**, 868 (2009).

[20] R. K. Vasudevan, W. Wu, J. R. Guest, A. P. Baddorf, A. N. Morozovska, E. A. Eliseev, N. Balke, V. Nagarajan, P. Maksymovych, and S. V. Kalinin, Domain wall conduction and polarization-mediated transport in ferroelectrics, Adv. Funct. Mater. **23**, 2592 (2013).

[21] J. Seidel, P. Maksymovych, Y. Bastra, A. Katan, S.-Y. Yang, Q. He, A. P. Baddorf, S. V. Kalinin, C.-H. Yang, J.-C. Yang, Y.-H. Chu, E. K. H. Salje, H. Wormeester, M. Salmeron, and R. Ramesh, Domain Wall Conductivity in La-doped $BiFeO_3$, Phys. Rev. Lett. **105**, 197603 (2010).

[22] W. Wu, J. R. Guest, Y. Horibe, S. Park, T. Choi, S. W. Cheong, and M. Bode, Polarization-Modulated Rectification at Ferroelectric Surfaces, Phys. Rev. Lett. **104**, 217601 (2010).

[23] E. A. Eliseev, A. N. Morozovska, G. S. Svechnikov, V. Gopalan, and V. Ya. Shur, Static conductivity of charged domain walls in uniaxial ferroelectric semiconductors, Phys. Rev. B **83**, 235313 (2011).

[24] E. A. Eliseev, A. N. Morozovska, G. S. Svechnikov, P. Maksymovych, and S. V. Kalinin, Domain wall conduction in multiaxial ferroelectrics, Phys. Rev. B **85**, 045312 (2012).

[25] M. Y. Gureev, A. K. Tagantsev, and N. Setter, Head-to-head and tail-to-tail 180 degrees domain walls in an isolated ferroelectric, Phys. Rev. B **83**, 184104 (2011).

[26] T. Keampfe, P. Reichenbach, M. Schreoder, A. Haussmann, and L. M. Eng, Optical three-dimensional profiling of charged domain walls in ferroelectrics by Cherenkov second-harmonic generation, Phys. Rev. B **89**, 035314 (2014).

[27] See Supplemental Materials at https://link.aps.org/supplemental/10.1103/PhysRevApplied.10.034002 for details of experiments and the simulation.

[28] J. A. Plascak and S. R. Salinas, Tunnelling model for quasi-one-dimensional hydrogen-bonded crystals, Phys. Status Solidi B **118**, 367 (1982).

[29] E. Matsushita, Tunneling mechanism on proton conduction in perovskite oxides, Solid State Ionics **145**, 445 (2001).

[30] T. Giamarchi and S. Bhattacharya, *High Magnetic Fields: Applications in Condensed Matter Physics and Spectroscopy*, edited by C. Berthier (Springer, Berlin, 2002), 314.

[31] B. Zieger, K. Martens, T. Giamarchi, and P. Paruch, Domain Wall Roughness in Stripe Phase $BiFeO_3$ Thin Films, Phys. Rev. Lett. **111**, 247604 (2013).

[32] J. Gonnissen, D. Batuk, G. F. Nataf, L. Jones, A. M. Abakumov, S. V. Aert, D. Schryvers, and E. K. H. Salje, Direct observation of ferroelectric domain walls in $LiNbO_3$: Wall-meanders, kinks, and local electric charges, Adv. Funct. Mater. **26**, 7599 (2016).

[33] Y. Du, H. Bo, Y. Kan, Y. Jin, X. Lu, T. Xu, S. Xiao, C. Yue, F. Huang, and J. Zhu, Domain growth and domain wall roughness along different directions in $LiNbO_3$ single crystal, J. Appl. Phys. **116**, 066814 (2014).

[34] Z. Xiao, J. Hamblin, S. Poddar, S. Ducharme, P. Paruch, and X. Hong, Effect of thermal annealing on ferroelectric domain structures in poly(vinylidene-fluoride-trifluorethylene) Langmuir-Blodgett thin films, J. Appl. Phys. **116**, 066819 (2014).

[35] S. C. Chae, Domain patterns and electric properties at domain walls in a surface normal to the direction of ferroelectric polarization in h-$ErMnO_3$, J. Korean Phys. Soc. **66**, 1381 (2015).